

Regulation mechanisms of electron-delocalized single transition metal-doped Mo_2CO_2 MXene hydrogen evolution reaction catalysts

Changxin Wang,^{1,2} Mei Yang,^{1,2} Shuo Cao,^{1,2} Xiaoxu Wang,^{3,4} Hao Fu,^{1,2} Yang Bai,^{1,2} Turab Lookman,⁵ Ping Qian,^{1,6,*} and Yanjing Su^{1,2,†,*}

¹Beijing Advanced Innovation Center for Materials Genome Engineering,
University of Science and Technology Beijing, Beijing 100083, China

²Corrosion and Protection Center, University of Science and Technology Beijing, Beijing 100083, China

³DP Technology, Beijing 100080, China

⁴AI for Science Institute, Beijing 100080, China

⁵Ai Materials Research LLC, Santa Fe, New Mexico 87501, USA

⁶Department of Physics, University of Science and Technology Beijing, Beijing 100083, China



(Received 11 March 2023; revised 12 July 2023; accepted 14 July 2023; published 2 August 2023)

Two-dimensional (2D) Mo-based MXenes ($\text{Mo}_{n+1}\text{C}_n\text{T}_x$) are recognized to have significant potential as hydrogen evolution reaction (HER) activity electrocatalysts. However, appropriate descriptors are absent to predict the H-adsorption Gibbs energy (ΔG_{H}) due to the unique delocalized electronic properties of the Mo atom. In this paper, we used first-principles calculations and machine learning to study the HER activity of Mo_2CO_2 with single transition metal-doped (Mo_2CO_2 -STM), and elucidate the mechanisms by which single transition metals (STMs) regulate the hydrogen evolution reaction. Our results revealed that ΔG_{H} has a “W” shape as a function of the doped atom changing in one period. The electronic structure analysis indicates that the electronic delocalized Mo has a longer range affecting not only the nearest atoms, but the second-nearest neighbor (STM-Mo) bonding effect controls the periodic distribution of ΔG_{H} . Using machine-learning method, we quantized the STM regulation mechanism using five key structural and electronic descriptors, and predicted the ΔG_{H} of Mo_2CO_2 -STM, which were also extended to W_2CO_2 -STM successfully. Our findings highlight the importance of considering second-nearest-neighbor bonding effects in similar delocalized materials systems research.

DOI: [10.1103/PhysRevMaterials.7.085801](https://doi.org/10.1103/PhysRevMaterials.7.085801)

I. INTRODUCTION

MXenes are a family of two-dimensional transition metal carbides and nitrides [1,2], with the general formula $M_{n+1}X_nT_x$ ($n = 1-4$), where M is a transition metal, X is C or N, and T represents surface functional groups such as O, OH, and F [3]. Due to their high electronic conductivity and high catalytic activity, MXenes have been successfully applied in various electrochemical applications, such as hydrogen evolution reaction (HER) [2,4], oxygen evolution reaction [5,6], supercapacitors [7], and metal ion batteries [8,9]. Among these materials, Mo-based MXenes ($\text{Mo}_{n+1}\text{C}_n\text{T}_x$) have been recognized as promising electrocatalysts [10–13], besides the widely studied Ti-based MXene materials [14,15]. Anasori *et al.* [16] reported that the H adsorption energy for Mo_2C is 0.048 eV, demonstrating its potential as an excellent HER electrocatalyst.

The hydrogen adsorption Gibbs energy (ΔG_{H}) is a commonly used descriptor for assessing the HER activity of electrocatalysts in theoretical investigations. However, calculating ΔG_{H} typically requires the total energies of materials

before and after hydrogen adsorption, which can be computationally expensive and time-consuming, especially when screening large numbers of candidate materials. To overcome this challenge, researchers can simplify the search for high-performance catalysts by identifying simple materials descriptors of catalyst before adsorption that can be used to predict ΔG_{H} . By reducing the computational costs of calculating ΔG_{H} , this approach can enable faster and more efficient screening of catalysts with desirable properties.

Doping with transition metal atoms [11,17] or matching different transition metal layers can change the surface electronic structure and chemical properties of Mo-based MXenes. But, the delocalization of d electrons of Mo makes the coupling effects between different atoms difficult to analyze. Moreover, it renders the traditional descriptors to predict H adsorption energy (ΔG_{H}) invalid. Kuznetsov *et al.* [18] observed that Co doping in Mo_2CT_x -Co led to changes in catalytic activity due to additional electron transfer between Co and O atom. Gan *et al.* [19] studied the -V, -Cr, -Mn, -Fe, -Co, -Ni, and -Cu loaded Mo_2CO_2 via first-principles calculations, and reported that the peak position in the density of states (DOS) of O atom is related to ΔG_{H} . Mo_2CO_2 exhibit extensive delocalization of Mo's d electrons [20] compared with other MXenes (Ti_2CO_2 , V_2CO_2). It makes the electrons of Mo more dispersive in space, which evidently changes the

*qianping@ustb.edu.cn

†yjsu@ustb.edu.cn

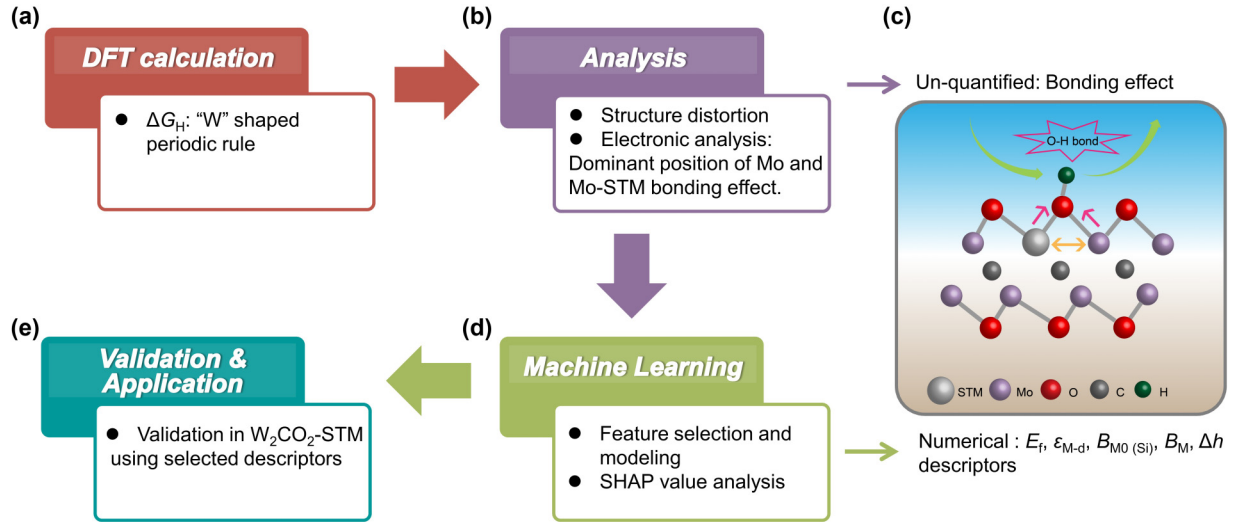


FIG. 1. Overall flow of MXene descriptors discovery.

adsorption performance of MXenes [21]. Anasori *et al.* [16] synthesized $\text{Mo}_2\text{TiC}_2\text{T}_x$ and found that in all cases and regardless of terminal, the DOS at the Fermi level of $\text{Mo}_2\text{TiC}_2\text{T}_x$ is mainly controlled by the d orbital of Mo, which makes conductivity of $\text{Mo}_2\text{TiC}_2\text{T}_x$ and $\text{Ti}_3\text{C}_2\text{T}_x$ entirely different [1,22]. We have previously [23] established one empirical equation model for the ΔG_{H} of single transition metal (STM)-doped MXenes (Ti, Zr, Ta, etc.) by using the bond length and Fermi level, but this model cannot be directly applied to Mo_2CO_2 -STM systems.

As one of the most important vacancies, the regulation mechanism between electronic-delocalization atom (Mo) and doped atoms, together with effective descriptors to quantize the mechanism, significantly restrict the development of new MXenes materials. Therefore, there is a need for in-depth research on the regulation mechanism of Mo-based MXenes. In this study, we used first-principles calculations and machine learning to investigate the size factor and electronic structure properties of Mo_2CO_2 with single transition metal atom-doped (Mo_2CO_2 -STM). We found that the delocalized electrons of Mo contribute to the bonding effect between the Mo atom and the next-nearest-neighbor STM atom, controlling the periodic distribution of ΔG_{H} . Additionally, we constructed a machine-learning model for predicting ΔG_{H} of Mo_2CO_2 -STM and identified five key descriptors. This model was successfully extended to W_2CO_2 -STM MXene materials, demonstrating its potential for identifying MXene materials with catalytic activity.

Figure 1 shows the overall flow of this work. First, in Fig. 1(a), the H catalytic activity of $3d$, $4d$, as well as $5d$ single transition metal-doped Mo_2CO_2 is calculated by density-functional theory DFT. The W-shaped periodic rule of doping tuned ΔG_{H} is discovered. Next, the reason underlying this rule at the structural and electronic levels is studied, as shown in Fig. 2(b), and we infer its origin in the long-range bond interaction of Mo and other atoms. To quantify this bond interaction [Fig. 2(c)], we build a machine-learning model with five descriptors: Fermi level (E_f), d -band center of STM atom ($\epsilon_{\text{M-d}}$), Bader charge of M_0 atom under the absorption site ($B_{M_0(\text{Si})}$), Bader charge of STM atom (B_M), and variation

of STM in z axis (Δh), which captures the trend in catalytic activity, and employ it to predict ΔG_{H} , as shown in Fig. 1(d). Finally, we extend these key descriptors to W_2CO_2 -STM to verify their validity in other MXenes with similar electronic delocalization, as shown in Fig. 1(e).

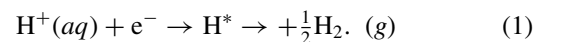
II. METHODS

A. *Ab initio* computation

The calculations were performed within the Vienna *Ab initio* Simulation Package (VASP) [24] based on DFT. The Perdew-Burke-Ernzerhof (PBE) functional within a generalized gradient approximation was used to express the exchange-correlation function [25]. The projector augmented-wave [26] method was applied to describe the pseudopotential. The cutoff kinetic energies for the plane waves were set to 600 eV for all the calculations. The convergence tolerance of the energy and force on each atom during structure relaxation were less than 10^{-4} eV and $0.001 \text{ eV \AA}^{-1}$, respectively. The energy calculations were performed with a $3 \times 3 \times 1$ supercell and with a total 20 Å vacuum for Mo_2CO_2 and Mo_2CO_2 -STM. The semiempirical dispersion-corrected DFT force-field approaches (DFT-D3) were adopted to describe the weak interaction involved in the calculations. The Fermi level was set into the center of the band gap following the convention. In addition, the integration crystal orbital Hamilton population (ICOHP) [27] is calculated by LOBSTER code [28], which can be used to quantitatively measure the bond strength between two atoms.

B. Gibbs free energy of hydrogen adsorption

The HER pathway of reaction can be described as



This reaction includes an initial state $\text{H}^+(aq) + e^-$, an intermediate state H^* , and a final state $\text{H}_2(g)$. The Gibbs free energy of the adsorption of the intermediate hydrogen on a catalyst (ΔG_{H}) is a key descriptor of the HER activity of the catalyst. When the pH and potential U effects are ignored,

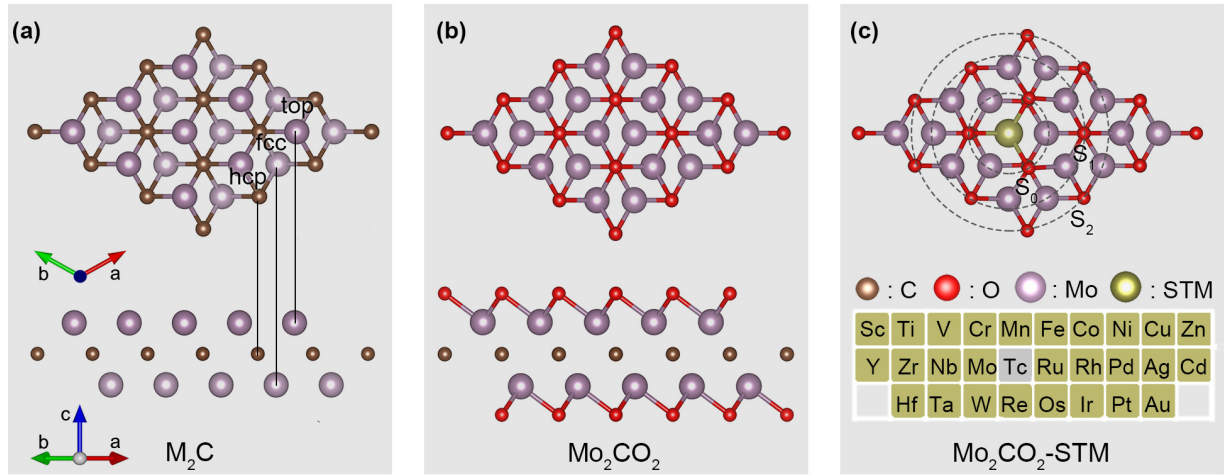


FIG. 2. Top and side views of $3 \times 3 \times 1$ supercell of Mo-based MXene structures. (a) M_2C structure: top, fcc and hcp represent the sites where O may be adsorbed; (b) Mo_2CO_2 with functional group O; (c) Single atom-doped model of Mo_2CO_2 -STM, STM = 3d, 4d, and 5d metals. S_0 , S_1 , and S_2 represent three types of O equivalent positions for H adsorption. Tc atom is excluded due to its radioactivity.

ΔG_H is defined as [29,30]

$$\Delta G_H = \Delta E_H + \Delta E_{ZPE} - T \Delta S_H, \quad (2)$$

where ΔE_H is the adsorption energy for adding one H atom onto the Mo_2CO_2 -STM catalysts. ZEP is zero-point energy. The ΔE_H is defined as

$$\Delta E_H = E_{H^*} - E_* - \frac{1}{2}E_{H_2}, \quad (3)$$

where E_{H^*} , E_* , and E_{H_2} are the total energies of the catalyst with one adsorbed H atom, the catalyst without any adsorbed H atom, and the total energies of H_2 for the gas phase, respectively. ΔE_{ZPE} and $T \Delta S_H$ in Eq. (2) are the difference in zero-point energy and the entropy between atomic hydrogen adsorption and hydrogen in the gas phase, respectively. ΔE_{ZPE} can be calculated using Eq. (4):

$$\Delta E_{ZPE} = E_{ZPE}^{H^*} - E_{ZPE}^* - \frac{1}{2}E_{ZPE}^{H_2}, \quad (4)$$

where the $E_{ZPE}^{H^*}$ and E_{ZPE}^* are, respectively, zero-point energy for the catalyst with one adsorbed H atom and the catalyst without any adsorbed H atom. The ΔS_H in Eq. (2) can be approximated as

$$\Delta S_H \approx \frac{1}{2}S_{H_2}^0, \quad (5)$$

because the vibrational entropy in the adsorbed state is minor according to previous studies [29], and $S_{H_2}^0$ is the entropy of H_2 gas under standard conditions. Here, the total values of $\Delta E_{ZPE} - T \Delta S_H$ for Mo_2CO_2 are listed as 0.366 eV in Table S1 [31]. Therefore, Eq. (2) can be written as

$$\Delta G_H = \Delta E_H + 0.366 \text{ eV}. \quad (6)$$

The optimal ΔG_H value for the HER is close to 0 eV, i.e., the smaller the $|\Delta G_H|$ value, the better the HER performance of the catalyst. The formation energy between the single transition metal atom and Mo vacancy defect (V_{Mo}) of Mo_2CO_2 substrates is defined as

$$E_{df} = E_{Mo_2CO_2-STM} - E_{Mo_2CO_2-V_{Mo}} - E_{STM}, \quad (7)$$

STM = 3d, 4d, and 5d metals,

where $E_{Mo_2CO_2-STM}$, $E_{Mo_2CO_2-V_{Mo}}$, and E_{STM} are the total energies of oxygen-terminated Mo vacancy defect MXenes with and without STM doping and the STM only, respectively. For a $3 \times 3 \times 1$ supercell, the STM-doped formation energy is evaluated as

$$E_{df} = E_{Mo_{17}C_9O_{18}-STM} - E_{Mo_{17}C_9O_{18}} - E_{STM}. \quad (8)$$

Equation (1) is dependent on the pH and the potential U through the chemical potential of H^+ and e^- , respectively. Therefore, the Gibbs free energy of the adsorption with potential U and pH effects is defined as

$$\Delta G_H^{pH} = \Delta G_H + \Delta G_U + \Delta G_{pH}. \quad (9)$$

ΔG_U is calculated by

$$\Delta G_U = -neU_{SHE}, \quad (10)$$

where n is the number of transferred electrons (here, $n = 1$ in HER) and e is the transferred charge. The standard hydrogen electrode potential (U_{SHE}) was theoretically defined in solution [$pH = 0$, $p(H_2) = 1 \text{ bar}$]. U is the applied electrode potential, which is at equilibrium, namely, $U = 0 \text{ V}$. Here, $\Delta G_U = 0 \text{ eV}$ [6].

ΔG_{pH} is defined as

$$\Delta G_{pH} = -k_B T \ln[H^+] = pH \times k_B T \ln 10, \quad (11)$$

where k_B is the Boltzmann constant, $k_B = 1.38 \times 10^{-23} \text{ J/K}$, and $T = 298.15 \text{ K}$. ΔG_H^{pH} vs pH is shown in Fig. S1 [31].

C. Kernel ridge regression

Kernel ridge regression (KRR) [32] combines ridge regression (linear least squares with l_2 -norm regularization) with the kernel trick [33]. It thus learns a linear function between the mapping space converted by the kernel and the target. The loss function of KRR can be the following:

$$loss = \sum_{i=1}^n \left(y_i - \sum_{j=1}^n \alpha_j \kappa(\vec{x}_j - \vec{x}_i) \right)^2 + \lambda \|\psi\|_2, \quad (12)$$

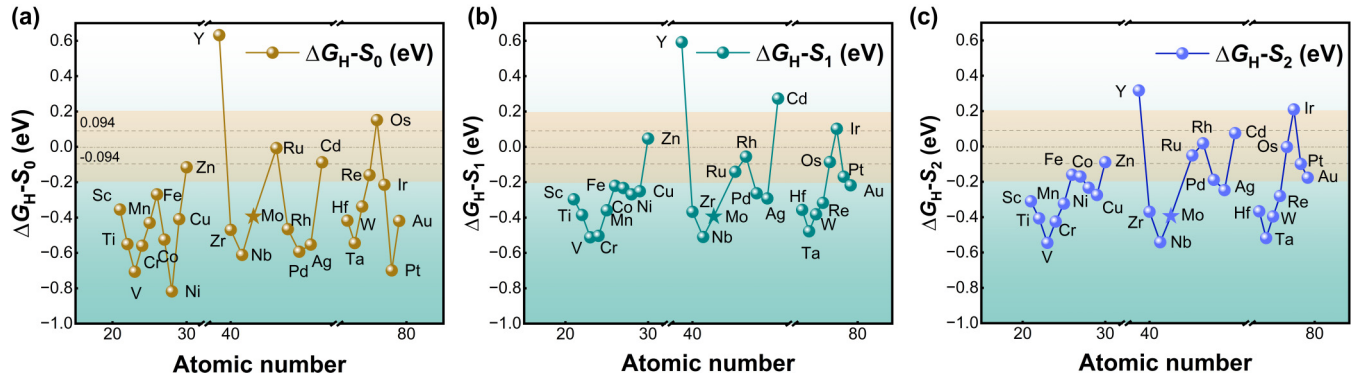


FIG. 3. ΔG_H of Mo_2CO_2 -STM. (a)–(c) ΔG_H of S_0 , S_1 , and S_2 sites. Dashed line near 0.094 eV is referencing ΔG_H of Pt(111) [38].

where the first part in Eq. (12) is the quadratic loss function and $\kappa(\vec{x}_j - \vec{x}_i)$ is a kernel function to map the input space to the higher-dimensional descriptor space. In this paper, the radial basis function (RBF) and Matern kernel are used [34]. The second part $\lambda\|\psi\|_2$ is the regularized term, which is the source of “ridge” in kernel ridge regression. The regularized item is used to balance the degree of fitting against the complexity of the model.

Four initial kernels are prepared for the KRR model, including standard RBF kernel, absolute exponential kernel (Matern kernel with smoothness coefficient 0.5), once-differentiable functions kernel (Matern kernel with smoothness coefficient 1.5), and twice-differentiable functions kernel (Matern kernel with smoothness coefficient 2.5). The λ and kernel optimization is implemented by Grid Search method. The whole machine-learning flow is built on the basis of opened SCIKIT-LEARN package [34].

III. MATERIALS

In Fig. 2(a), the initial M_2C (M is a transition metal, such as Mo, Ti, Zr, etc.) possesses a uniform three-layer structure. As shown in Fig. 2(b), terminal functional groups O are loaded onto the surface of Mo_2C to form Mo_2CO_2 structures, which can considerably improve the surface activity. The selection of O terminal functional groups is based on their thermodynamic stability, as they are more stable than OH terminal functional groups [35]. It is worth acknowledging that certain studies [36,37] suggest that MXenes with a combination of H/OH terminal functional groups exhibit superior stability. However, due to the presence of multiple types of adsorption sites and local structures introduced by the relative position of the doped element, H, and OH, this paper does not consider the utilization of mixed terminal functional groups.

The positions in which the terminal groups could be located are classified as top, face-centered cubic (fcc), and hexagonal close-packed (hcp). For Mo_2CO_2 , the hcp position is the most stable site for the O atom, and the calculation process is presented in detail in Table S2 and Table S3 [31].

As shown in Fig. 2(c), the Mo atom in Mo_2CO_2 -STM is substituted by STM. Here, STM represents 27 different transition metals, among which Tc is excluded due to its radioactivity. After the single-atom replacement, the O atoms capable of adsorbing H are no longer equivalent, due to the different relative distance influence of the replacement atom.

Therefore, the relative distance from the replacement atom is used to distinguish the three types of positions of S_0 , S_1 , and S_2 , as shown in Fig. 2(c).

IV. RESULTS

A. Adsorption Gibbs free energy

Figures 3(a)–3(c) illustrate the ΔG_H of Mo_2CO_2 -STM. The ΔG_H value at position S_0 displays noticeable periodicity with the periodic row of the transition metal. Specifically, as the atomic number of the STM increases, the ΔG_H curve exhibits a W-shape variation within a single period (row), indicating that ΔG_H of Mo_2CO_2 -STM can be affected by numerous factors. Similar trends in ΔG_H are also observed for the S_1 and S_2 positions. By comparing Figs. 3(a)–3(c), the variance of ΔG_H decreases as the distance between the catalytic site and the doped atom increases, suggesting that the influence of the doped atom on the adsorption site becomes weaker with distance.

As shown in Figs. 3(a)–3(c), the ΔG_H of S_0 , S_1 , S_2 sites of Mo_2CO_2 -Zn, Mo_2CO_2 -Ru, and Mo_2CO_2 -Os fall within the range of -0.2 to 0.2 eV, which indicates that these materials possess high catalytic efficiency and significant exploration potential. The relationship between exchange current and ΔG_H , considering the influence of kinetics [39,40], is discussed and illustrated in Supplemental Material, Text S1 [31].

B. Structure analysis

The size factors Δh and Δr in Fig. 4 are used to reflect the volume distortion caused by the introduction of STM atoms. Δh represents the difference in the z direction between the STM and the replaced Mo atom, which reflects the upward and downward movement of the STM relative to the surface. As shown in Fig. 4(c), the value of Δh is directly related to the atomic number of the STM atom because the atomic radius of each element in the periodic table row corresponds to a fall and rise pattern. When the STM is compressed due to interactions with surrounding atoms, Δh increases, causing the STM to be pushed to the surface, even beyond the surface to form an STM protrusion if its size is greater than 1.2 \AA . Furthermore, post-transition metals such as Zn and Cd have high Δh values. This can be attributed to the filling of the d band of post-transition metals, which intensifies the shielding effect and leads to a drop in the outer-layer electron binding,

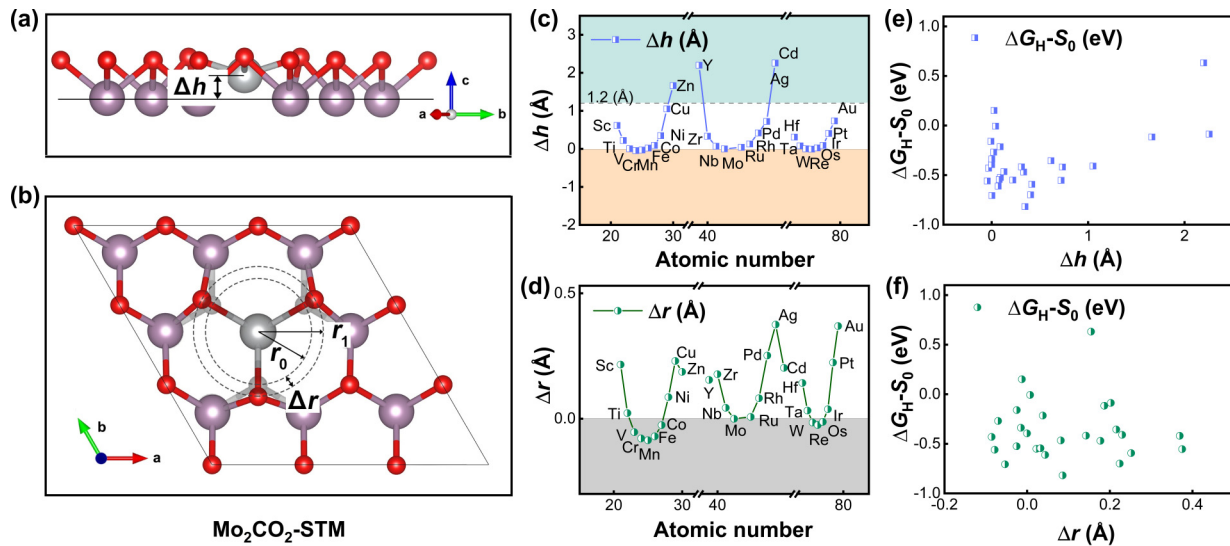


FIG. 4. Structure changes after STM doping. (a) Δh : z-axis distance difference between STM and replaced Mo; (b) Δr : distance difference after and before STM doped between S_0 site and STM in (0,0,1) face; (c) Δh vs atomic number of STM atom; (d) Δr vs atomic number of STM atom. (e) ΔG_{H} of S_0 sites vs Δh ; (f) ΔG_{H} of S_0 sites vs Δr .

resulting in an increase in radius. As a result, these elements require more space to accommodate the electron cloud, and the STM atom is pushed further from the surface.

The parameter r_0 is the horizontal distance between the O atom at the S_0 site and the STM on the (0,0,1) plane as depicted by the dotted circles in Fig. 4(b). Δr is the difference in r_0 observed before and after STM doping, and is utilized to reflect the influence of STM on the O atom. Negative Δr values signify a reduction in the O atom's size towards the center. Figure 4(d) highlights the behavior of Δr , which also exhibits a “U” shape along atomic numbers in a given period. This pattern is attributed to the periodic changes in the radius of the STM atoms. Notably, Zn, Y, and Cd atoms are extruded out due to internal extrusion stress at the surface, which causes a decrease in Δr values.

As shown in Figs. 4(e) and 4(f), there is no direct correlation between the two size factors and the adsorption energy curve. Therefore, the size factor alone cannot reflect the adsorption energy of Mo_2CO_2 -STM systems.

C. Electronic analysis

Figure 5 presents the projected density of states (PDOS) of atoms in the Mo_2CO_2 -STM system. The peaks of STM- d -PDOS move to the left as the group number of STM increases in total. In Fig. 5(a), we observe that the peaks of STM- d -PDOS shift to lower energies as the group number increases. Further analysis of the PDOS curves reveals that STM- d -PDOS exhibits slight oscillations between 0 and -6.5 eV. STM- d -PDOS fluctuate slightly from 0 to -2 , -4.5 , and -6.5 eV.

As shown in Fig. 5(b), C- p -PDOS form peaks in -3 and -6.5 eV, respectively. Notably, the main peaks of Mo- d -PDOS are located at -4.5 eV, and show a broad distribution in energy space. The peaks of all O- p -PDOS are around -4.5 eV in Fig. 5(d). At the same energy level, the PDOS peaks of STM, O, and Mo atoms overlap, making it

challenging to assign the specific atom responsible for the observed interactions at -4.5 eV based solely on PDOS analysis.

Therefore, we use crystal orbital Hamilton population (COHP) analysis to further obtain the bonding and antibonding effects between superficial atoms of Mo_2CO_2 -STM. COHP analyzes the interaction between energy orbital of energy band structure, and is used to represent the contribution of bonding and antibonding to energy band structure: COHP < 0 means bonding, and COHP > 0 means antibonding. To quantify the strength of the bonding interaction, we integrate the COHP curve from minus infinity to the Fermi level, resulting in an integration crystal orbital Hamilton population (ICOHP) value. Typically, the value of $-\text{ICOHP}$ is used to quantify bond strength.

The trends in the $-\text{ICOHP}$ values of the fourth period can be observed in Fig. 6. We note that the $-\text{ICOHP}_{(\text{STM}-\text{O})}$ values decrease with an increase in atomic number, and an inflection point occurs at the Ni site. $-\text{ICOHP}_{(\text{Mo}-\text{O})}$ remain nearly flat, with a slow rise over a period. The trend for STM-Mo bonding is characterized by several evident inflection points. $-\text{ICOHP}_{(\text{STM}-\text{Mo})}$ values display a minimum of two inflection points within each period. In the fourth period, we observe Fe and Ni inflection points. We note that the trends for $-\text{ICOHP}_{(\text{STM}-\text{O})}$, $-\text{ICOHP}_{(\text{Mo}-\text{O})}$, and $-\text{ICOHP}_{(\text{STM}-\text{Mo})}$ are similar across periods 4, 5, and 6.

In electron localized systems, such as Ti_2CO_2 MXenes, the interaction of the second-nearest neighbor between STM and the base metal (Ti, Mo, etc.) is usually not considered. However, an examination of Fig. 6 shows that $-\text{ICOHP}$ values for both STM-O [Fig. 6(a)] and STM-Mo [Fig. 6(c)] are equally significant. This finding suggests that the bonding effect of STM-Mo in Mo_2CO_2 is non-negligible. Figure S2 [31] provides additional comparisons of the three MXene-STM systems. Consequently, our focus is directed towards the STM-Mo bond.

Figure S3 [31] shows the COHP line details of STM-Mo, indicating the action region of bonding and antibonding

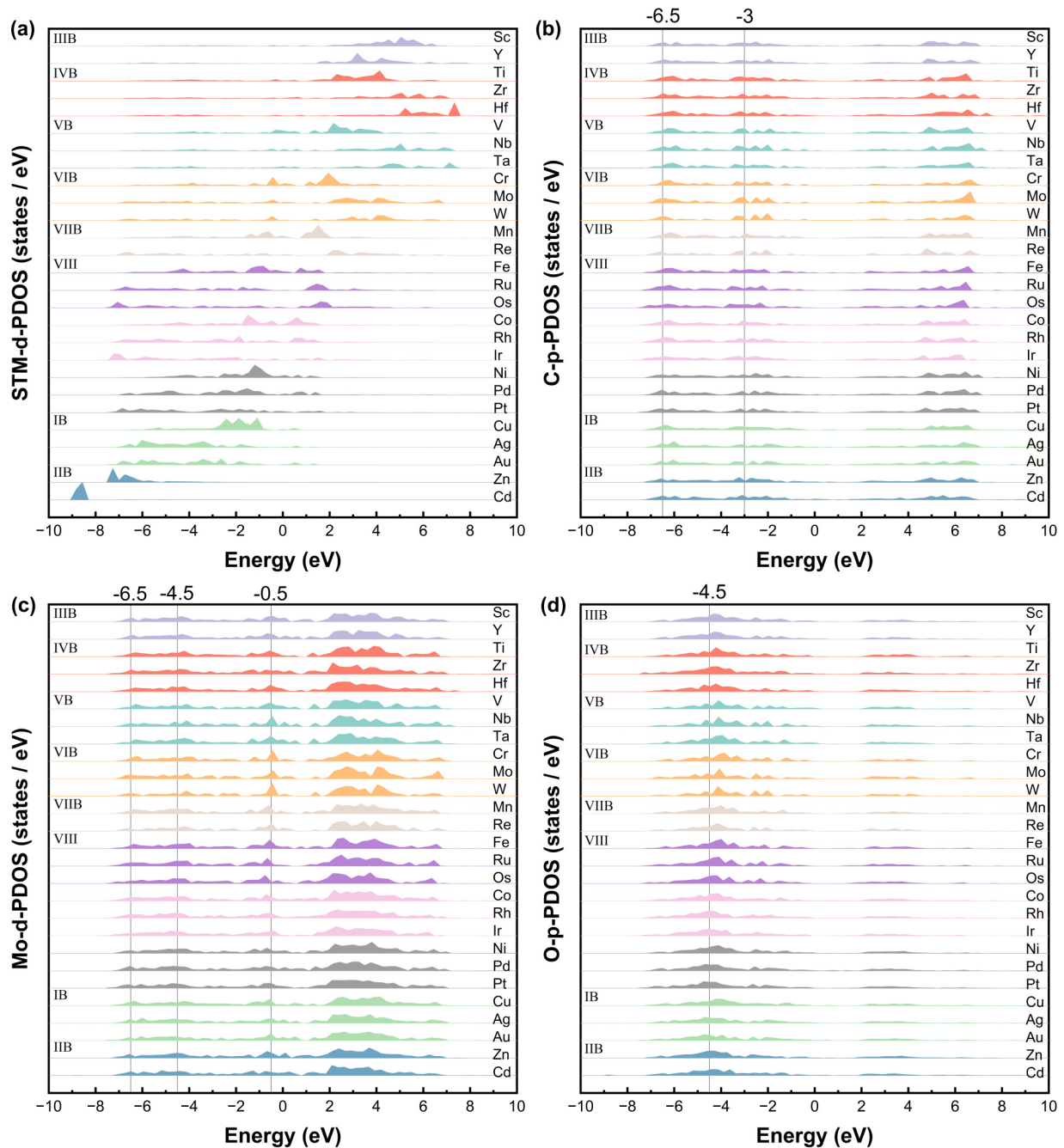


FIG. 5. PDOS of atoms in $\text{Mo}_2\text{CO}_2\text{-STM}$. (a) STM-*d*-PDOS; (b) C-*p*-PDOS; (c) Mo-*d*-PDOS; and (d) O-*p*-PDOS.

interactions. This study emphasizes the bonding region of the COHP lines that lie below the zero-scale line of the y axis. Figure S3 depicts that, taking the fourth period as an example, the primary bonding region between STM and Mo shifts towards the left and disappears as atomic number increases. It occurs within a range of 0 to -2 eV. The second bonding region emerges in the -4.5 eV region as the atomic number increases, reaches its maximum at the V atom, and later vanishes near the Fe and Co atoms. The third bonding region appears near -6.5 eV, commencing at the Fe atom, reaching its maximum at the Ni atom, and then diminishing.

The crucial points of change in the bonding region (V, Fe, Ni) correspond to the inflection points of $-\text{ICOHP}_{(\text{STM}-\text{O})}$

and $-\text{ICOHP}_{(\text{STM}-\text{Mo})}$ curves in Fig. 6, and more importantly, the critical nodes of the trend line ΔG_{H} in Fig. 2. This observation indicates that the bonding between STM-Mo may be the key factor influencing the change in the ΔG_{H} trend.

Figure 6(a) shows that the PDOS peaks of the fifth- and sixth period atoms occur within the -6.5 and -4 eV range. The $-\text{ICOHP}_{(\text{STM}-\text{O})}$ and $-\text{ICOHP}_{(\text{STM}-\text{Mo})}$ trends for the fifth- and sixth period atoms exhibit a tendency similar to that of the fourth period atoms, except for the Y atom, which is located above the outer O surface. However, the rules of $\text{ICOHP}_{(\text{STM}-\text{O})}$ and $\text{ICOHP}_{(\text{STM}-\text{Mo})}$ for the fifth- and sixth period atoms become less apparent when considering the influence of the C-*p* orbital near -6.5 eV.

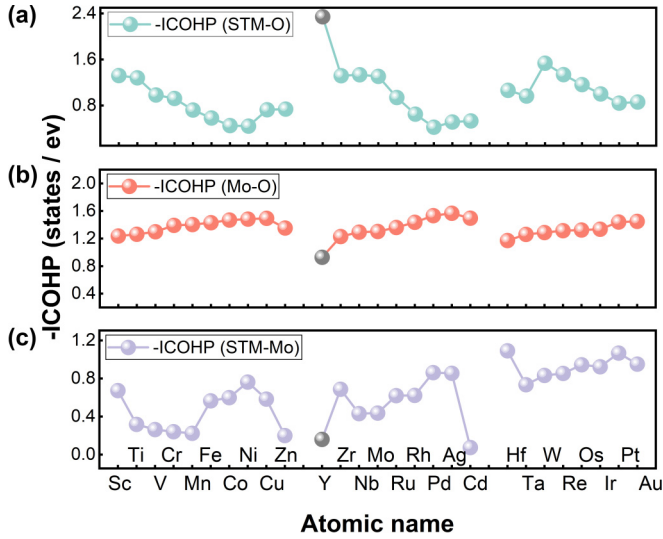


FIG. 6. $-ICOHP$ values: (a) $-ICOHP_{(STM-O)}$; (b) $-ICOHP_{(Mo-O)}$; and (c) $-ICOHP_{(STM-Mo)}$.

With the peaks of STM- d -PDOS shifting to the left in each period, the STM atom interacts sequentially with other atoms (O, Mo, C) at the -2 , -4.5 , and -6 eV sites. The asynchrony of these orbital interactions leads to multiple inflection points (such as V, Fe, Ni, etc.) in the STM-O and STM-Mo bonding curves within a single period. When H is absorbed on the surface, the O-H bond is influenced by the coupling effect of the underlying atoms and bonds; the bonds with periodic variation of STM-O and STM-Mo affect the formation of the O-H bond, so the inflection points above remain in the O-H bond change curve. As a result, the ΔG_H exhibits a W-shape variation. The strong STM-Mo bonding effect is likely the reason for the unique hydrogen evolution performance of Mo-based MXenes.

D. Machine learning

Since the ICOHP calculation is time-consuming and using a single descriptor may not be enough to accurately predict ΔG_H , we employed machine-learning methods to identify key descriptors for Mo-based MXenes HER catalytic activity [44,45]. We extracted 18 descriptors from 27 Mo_2CO_2 -STM structures before H absorption, based on previous suggestions

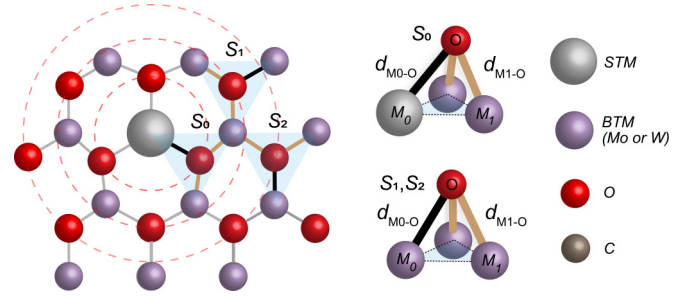


FIG. 7. Mo_2CO_2 -STM bonds. Types of M_0 -O bonds (black) at S_0 , S_1 , and S_2 sites are STM-O, BTM-O, and BTM-O, respectively, and the bonds of M_1 -O (brown) at S_0 , S_1 , and S_2 sites are all BTM-O. BTM is defined as base transition metal, and as stated, STM is defined as single transition metal.

for descriptors in the literature [44,46–48]. Using these descriptors, we built machine-learning (ML) models to predict ΔG_H .

The initial descriptors used in this study mainly reflect the bonding effects and are listed in Table I. Each descriptor can be represented by a single numerical value. The descriptors with complex numerical matrix representation, like SOAP [49] and Coulomb Matrix [50], were not considered in this study. We defined the base transition metal (Mo) in MXenes as BTM and the doped single transition metal as STM to better distinguish the transition atoms. Additionally, for the bonds around the O adsorption site, we defined the distinct bond as M_0 -O and the other two equivalent bonds as M_1 -O, as shown in Fig. 7. The relational graphs between ΔG_H and typical descriptors are shown in Fig. S4 [31].

Each Mo_2CO_2 -STM structure produces three Mo_2CO_2 -STM-H- S_i structures after absorption, due to the difference of adsorption sites. Therefore, the properties of local structure near these three potential adsorption sites in Mo_2CO_2 -STM structure are distinguished. The S_i label ($i = 0-2$) indicates that the descriptors take different values at the S_0 , S_1 , and S_2 potential adsorption sites of Mo_2CO_2 -STM structure, as shown in Table I.

To select descriptors related to ΔG_H , the study applied correlation-coefficient screening to the 18 descriptors shown in Fig. S5 [31], and the descriptor ε_{BTM-d} was filtered out due to its strong correlation with ε_{M-d} . We enumerated all the possible descriptor combinations of the remaining 17

TABLE I. Eighteen primary descriptors associated with elemental and geometrical properties that are calculated by DFT-PBE or simple processing.

Symbol	Name	Symbol	Name
$d_{M_0-O(S_i)}$	M_0 -O distance in MXene	ε_{M-d}	d -band center of STM
$d_{M_1-O(S_i)}$	M_1 -O distance in MXene	ε_{BTM-d}	d -band center of BTM (average)
Δh	Height movement of STM	ε_{O-p}	p -band center of O (average)
Δr	Radius difference of the adsorption	B_M	Bader charge of STM (S_0)
R_M	Ionic radius of STM	B_{BTM}	Bader charge of BTM (S_0)
χ_M	Pauling electronegativity of STM	B_O	Bader charge of O (S_0)
Z_M	Nuclear charge number of STM	B_C	Bader charge of C (S_0)
E_g	Band gap using PBE	$B_{M_0(S_i)}$	Bader charge of M_0
E_f	Fermi level in MXene	$B_{O(S_i)}$	Bader charge of O

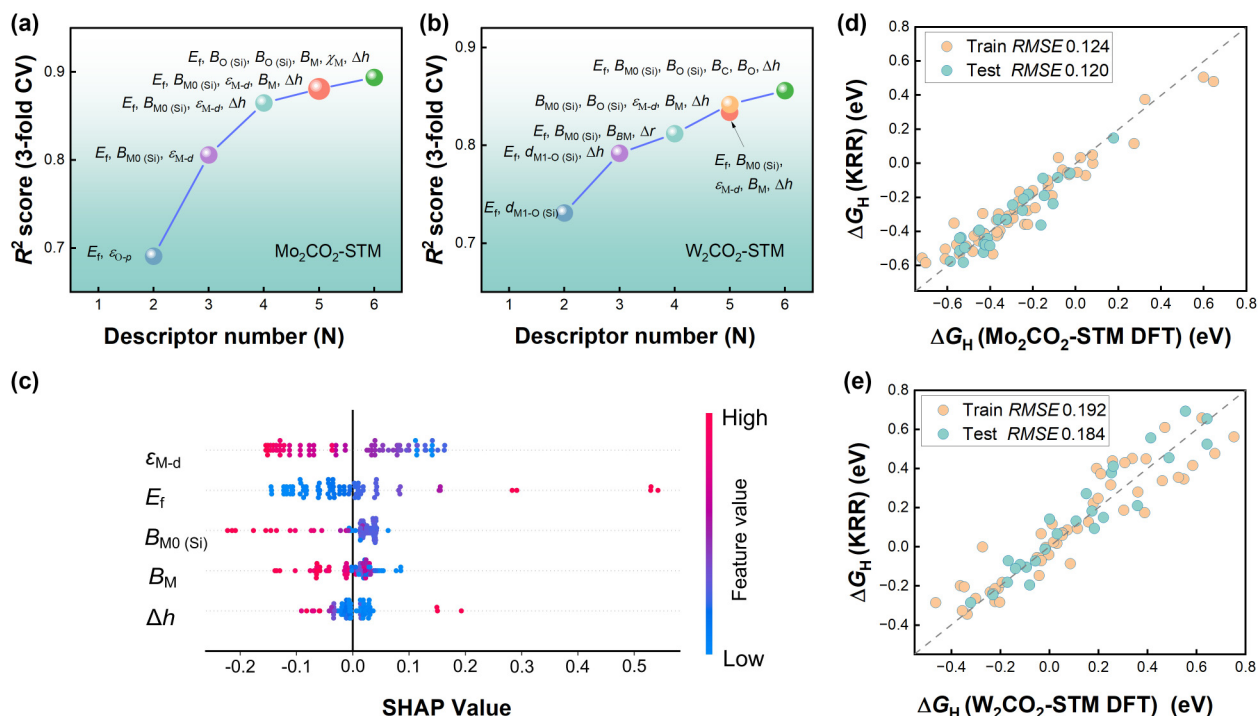


FIG. 8. Machine-learning results. (a) Feature selection for $\text{Mo}_2\text{CO}_2\text{-STM}$; (b) Feature selection for $\text{W}_2\text{CO}_2\text{-STM}$; (c) SHAP values for five key descriptors of $\text{Mo}_2\text{CO}_2\text{-STM}$; (d) ΔG_H predicted by KRR model for $\text{Mo}_2\text{CO}_2\text{-STM}$ with five key descriptors; and (e) ΔG_H predicted by KRR model for $\text{W}_2\text{CO}_2\text{-STM}$ with five key descriptors.

descriptors and trained ML models based on a $\text{Mo}_2\text{CO}_2\text{-STM}$ dataset of 81 points to find the subset of descriptor with the threefold cross-validation (CV) error [34]. The training set consisted of 54 samples (67%), with the remaining 27 samples (33%) used as test data, and both R^2 (decision coefficient) and $RMSE$ (root-mean-square error) were monitored during the process. The performance of different numbers of descriptors in the KRR machine learning model is shown in Fig. 7. The details of the combination of descriptors and their R^2 scores and $RMSE$ errors are shown in Table S4 [31].

From Fig. 8(a), the R^2 score (CV) increases rapidly with an increasing number of descriptors (N) up to 5, after which the increase slows down. Therefore, it is reasonable to choose five descriptors as the final descriptors to retain the simplicity of the model. The subsets of descriptors with $2 < N < 6$ all included the Fermi level (E_f), d -band center of STM (ϵ_{M-d}), as well as the Bader charge of M_0 in three sites ($B_{M0(Si)}$). The descriptors Δh and B_M were consistently ranked fourth and fifth, respectively. Across the different subsets of the descriptors, their rankings remained stable across the range of N . Based on these findings, the final set of descriptors selected for the model were E_f , ϵ_{M-d} , $B_{M0(Si)}$, Δh , and B_M .

To further demonstrate the efficacy of the selected descriptors to model HER materials, we applied them to another unlocalized-electron system, $\text{W}_2\text{CO}_2\text{-STM}$, since metallic tungsten dioxide (WO_2) is also known to have a W-metal bonding effect [51]. The specific combinations of descriptors and corresponding errors are presented in Table S5 [31]. As illustrated in Fig. 8(b), we repeated the feature selection process on $\text{W}_2\text{CO}_2\text{-STM}$ in the same manner as that done for $\text{Mo}_2\text{CO}_2\text{-STM}$. Interestingly, the five descriptors selected for $\text{W}_2\text{CO}_2\text{-STM}$ were only different by one

descriptor from those selected for $\text{Mo}_2\text{CO}_2\text{-STM}$. Therefore, we modeled $\text{W}_2\text{CO}_2\text{-STM}$ with E_f , ϵ_{M-d} , $B_{M0(Si)}$, Δh , and B_M descriptors and find these five descriptors selected by $\text{Mo}_2\text{CO}_2\text{-STM}$ differ by 0.03 R^2 from those selected by $\text{W}_2\text{CO}_2\text{-STM}$. The five descriptors generalize well, suggesting that the unlocalized-electron MXene system may behave similarly as $\text{Mo}_2\text{CO}_2\text{-STM}$.

To elucidate the impact of descriptors on the model prediction, we generated a plot of SHAP (SHapley Additive exPlanations) analysis [52], which is an algorithm for interpreting predictions. As presented in Fig. 8(c), each point in the plot represents one MXene sample, and the color indicates the normalized value of the corresponding descriptor. Specifically, red signifies that the value is larger than the mean of the descriptor, while blue signifies that the value is smaller. SHAP values indicate the positive or negative influence of each sample on ΔG_H when considering individual descriptors. Generally, a wider distribution of SHAP values for a descriptor denotes its greater significance.

Different from the feature selection results above, the SHAP method ranked the ϵ_{M-d} as the most important descriptor. It is reasonable because ϵ_{M-d} is the original factor of STM doping. It reflects the interaction of the d orbital of STM with the orbitals of other atoms (O, Mo, C), causing changes in ΔG_H periodically. The ϵ_{M-d} exhibits a negative relationship with ΔG_H , where a higher d -band center indicates a more negative ΔG_H [53]. This is consistent with the d -band center theory [54]. Generally, as the center of the d orbital rises, the antibonding state is forced to rise above the Fermi level, causing a decrease in electron filling of the antibonding state, leading to a stronger bond between the adsorb atom and the catalyst surface, resulting in a more negative ΔG_H .

In the HER catalytic activity problem, E_f exhibits strong stability across all descriptors, which is consistent with Ref. [23]. Among the samples with high E_f values, approximately seven (shown in red color) exhibit large positive SHAP values. This indicates that for these samples, E_f is an important predictor for the model.

$B_{M_0(S_i)}$ exhibits a strong negative correlation with ΔG_H , where less electron loss of center atoms M_0 (represented in red color) leads to a more negative ΔG_H . The blue “block” for $B_{M_0(S_i)}$ represents samples where electron transformation is small, and these samples provide little information for the model ($0 < \text{SHAP value} < 0.05$). The reason for this phenomenon is that $B_{M_0(S_i)}$ reflects the amount of charge transferred from the metal atom in different absorption sites, and is a key descriptor that directly reflects the local structure differences of S_0 , S_1 , and S_2 sites. The number of electrons that are gained by the O atom from the metal atoms before hydrogen adsorption, known as the O-atom gains [55], have been shown to impact the hydrogen and oxygen bonds during adsorption. If the O atom receives fewer electrons from the underlying metal atoms, it is more likely to obtain electrons from H atoms during the hydrogen adsorption process. This results in a stronger O–H bond, leading to a more negative ΔG_H . When the electron loss of center atoms M_0 is similar to the electron loss of Mo atoms, as in the blue-block samples, it becomes difficult to distinguish them using $B_{M_0(S_i)}$.

The B_M is the Bader charge of STM atom. The same trend that $B_{M_0(S_i)}$, B_M , and $B_{M_0(S_i)}$ are selected at the same time because they are complementary to each other is shown. B_M reflects the unique charge distribution of different center STM atoms. Therefore, B_M is an information supplement to $B_{M_0(S_i)}$ and helps improve the accuracy of the model by providing additional information on the charge distribution of STM atoms.

Different from the former four descriptors, Δh shows a nonmonotonic correlation with ΔG_H . Samples with large Δh (represented in red color) are valuable data for model prediction, as they help to distinguish different structures. In contrast, samples with smaller Δh , corresponding to the blue points of the Δh descriptor in Fig. 8 and the points of valley in Fig. 4(c), are almost useless for modeling if considering only the Δh descriptor. This is because the structures for these samples are close to the initial Mo_2CO_2 structure. Therefore, while Δh is an important descriptor, its relationship with ΔG_H is nonmonotonic and should be considered alongside the other descriptors for accurate model prediction.

Based on the five descriptors, a KRR model was trained using 54 random samples and tested on the remaining 27

samples in Mo_2CO_2 -STM, with an R^2 value of 0.904 for the training data and 0.884 for the testing data, as shown in shown in Fig. 8(d). A similar model was also trained for W_2CO_2 -STM, with R^2 values of 0.856 for both the training and 0.833 for testing data [Fig. 8(e)]. To provide the uncertainty with the prediction by machine-learning model, we retrained Gaussian process regression (GPR) model by five key descriptors in the Supplemental Material [31], which also proved good application effect of the feature five descriptors.

Compared to previously explored MXenes-STM [23], which used E_f and $d_{M1-O(S_i)}$ as descriptors for Ti_2CO_2 -STM, Zr_2CO_2 -STM, and Ta_2CO_2 -STM, the five descriptors in this paper provide more information for describing the complicated electronic structure information of Mo_2CO_2 -STM and W_2CO_2 -STM. The dispersion distribution of Mo electrons introduces the interaction with second-nearest-neighbor atoms, which requires more descriptors to be used for an accurate model. Therefore, d -band center and Bader charge are promising electronic descriptors that can be developed further to improve the accuracy of the model.

V. CONCLUSION

In this study, we investigated the size factor and electronic structure properties of single transition metal atom-doped Mo_2CO_2 MXenes using first-principles calculations and machine-learning methods. We found that Mo_2CO_2 -Ru, Mo_2CO_2 -Zn, and Mo_2CO_2 -Os have ΔG_H values in the range of -0.2 to 0.2 eV, which suggests their potential as HER catalysts. We also identified five key descriptors (E_f , ε_{M-d} , $B_{M_0(S_i)}$, Δh , and B_M) that can be used to predict ΔG_H in Mo_2CO_2 -STM by machine-learning screening in delocalized-electron MXenes. The relevance of our findings was also confirmed in W_2CO_2 -STM systems. Finally, we highlighted the importance of considering the second-nearest neighbor bonding effect for Mo and W atoms not only in MXene materials but also in catalytic materials.

Authors can confirm that all relevant data are included in the paper and or its Supplemental Material files.

ACKNOWLEDGMENT

The authors gratefully acknowledge the financial support of The National Key Research and Development Program of China (Grant No. 2021YFB3500700).

The authors declare no conflict of interest.

- [1] M. Naguib, M. Kurtoglu, V. Presser, J. Lu, J. Niu, M. Heon, L. Hultman, Y. Gogotsi, and M. W. Barsoum, Two-dimensional nanocrystals produced by exfoliation of Ti_3AlC_2 , *Adv. Mater.* **23**, 4248 (2011).
- [2] C. Ling, L. Shi, Y. Ouyang, Q. Chen, and J. Wang, Transition metal-promoted V_2CO_2 (MXenes): A new and highly active catalyst for hydrogen evolution reaction, *Adv. Sci.* **3**, 1600180 (2016).
- [3] J. Suntivich, H. A. Gasteiger, N. Yabuuchi, H. Nakanishi, J. B. Goodenough, and Y. Shao-Horn, Design principles for

oxygen-reduction activity on perovskite oxide catalysts for fuel cells and metal-air batteries, *Nat. Chem.* **3**, 546 (2011).

- [4] B. Huang, N. Zhou, X. Chen, W. J. Ong, and N. Li, Insights into the electrocatalytic hydrogen evolution reaction mechanism on two-dimensional transition-metal carbonitrides (MXene), *Chem. - A Eur. J.* **24**, 18479 (2018).
- [5] T. Y. Ma, J. L. Cao, M. Jaroniec, and S. Z. Qiao, Interacting carbon nitride and titanium carbide nanosheets for high-performance oxygen evolution, *Angew. Chem.* **128**, 1150 (2016).

- [6] B. Mohanty, P. Bhanja, and B. K. Jena, An overview on advances in design and development of materials for electrochemical generation of hydrogen and oxygen, *Mater. Today Energy* **23**, 100902 (2022).
- [7] M. R. Lukatskaya, O. Mashtalir, C. E. Ren, Y. Dall'Agnese, P. Rozier, P. L. Taberna, M. Naguib, P. Simon, M. W. Barsoum, and Y. Gogotsi, cation intercalation and high volumetric capacitance of two-dimensional titanium carbide, *Science* **341**, 1502 (2013).
- [8] N. Li, Y. Li, X. Zhu, C. Huang, J. J. Kai, and J. Fan, Theoretical investigation of the structure-property correlation of MXenes as anode materials for alkali metal ion batteries, *J. Phys. Chem. C* **124**, 14978 (2020).
- [9] X. Tang, D. Zhou, P. Li, X. Guo, B. Sun, H. Liu, K. Yan, Y. Gogotsi, and G. Wang, MXene-based dendrite-free potassium metal batteries, *Adv. Mater.* **32**, 1906739 (2020).
- [10] S. Wang, L. Chen, Y. Wu, and Q. Zhang, Surface modifications of Ti_2CO_2 for obtaining high hydrogen evolution reaction activity and conductivity: A computational approach, *ChemPhysChem* **19**, 3380 (2018).
- [11] C. Wang, S. Chen, and L. Song, Tuning 2D MXenes by surface controlling and interlayer engineering: Methods, properties, and synchrotron radiation characterizations, *Adv. Funct. Mater.* **30**, 2000869 (2020).
- [12] M. K. Aslam, Y. Niu, and M. Xu, MXenes for non-lithium-ion (Na, K, Ca, Mg, and Al) batteries and supercapacitors, *Adv. Energy Mater.* **11**, 2000681 (2021).
- [13] N. Li, X. Chen, W. J. Ong, D. R. Macfarlane, X. Zhao, A. K. Cheetham, and C. Sun, Understanding of electrochemical mechanisms for CO_2 capture and conversion into hydrocarbon fuels in transition-metal carbides (MXenes), *ACS Nano* **11**, 10825 (2017).
- [14] Y. Cheng, L. Wang, Y. Song, and Y. Zhang, Deep insights into the exfoliation properties of MAX to MXenes and the hydrogen evolution performances of 2D MXenes, *J. Mater. Chem. A* **7**, 15862 (2019).
- [15] Y. Jiang, T. Sun, X. Xie, W. Jiang, J. Li, B. Tian, and C. Su, Oxygen-functionalized ultrathin $Ti_3C_2T_x$ MXene for enhanced electrocatalytic hydrogen evolution, *ChemSusChem* **12**, 1368 (2019).
- [16] B. Anasori, Y. Xie, M. Beidaghi, J. Lu, B. C. Hosler, L. Hultman, P. R. C. Kent, Y. Gogotsi, and M. W. Barsoum, Two-Dimensional, ordered, double transition metals carbides (MXenes), *ACS Nano* **9**, 9507 (2015).
- [17] Y. Gao, Y. Cao, Y. Gu, H. Zhuo, G. Zhuang, S. Deng, X. Zhong, Z. Wei, J. Chen, Xiang-Pan, and J-g. Wang, Functionalization Ti_3C_2 MXene by the adsorption or substitution of single metal atom, *Appl. Surf. Sci.* **465**, 911 (2019).
- [18] D. A. Kuznetsov, Z. Chen, P. V. Kumar, A. Tsoukalou, A. Kierzkowska, P. M. Abdala, O. V. Safonova, A. Fedorov, and C. R. Müller, Single site cobalt substitution in 2D molybdenum carbide (MXene) enhances catalytic activity in the hydrogen evolution reaction, *J. Am. Chem. Soc.* **141**, 17809 (2019).
- [19] J. Gan, F. Li, Y. Tang, and Q. Tang, Theoretical study of transition-metal-modified Mo_2CO_2 MXene as a catalyst for the hydrogen evolution reaction, *ChemSusChem* **13**, 6005 (2020).
- [20] Z. Zhu, S. Chowdhary, V. C. Long, J. L. Musfeldt, H.-J. Koo, M.-H. Whangbo, X. Wei, H. Negishi, M. Inoue, J. Sarrao, and Z. Fisk, Polarized optical reflectance and electronic structure of the charge-density-wave materials Mo_4O_{11} , *Phys. Rev. B* **61**, 10057 (2000).
- [21] Y. Xiao and W. Zhang, Adsorption mechanisms of Mo_2Cr_2 MXenes as potential anode materials for metal-ion batteries: A first-principles investigation, *Appl. Surf. Sci.* **513**, 145883 (2020).
- [22] Z. K. Han, D. Sarker, R. Ouyang, A. Mazheika, Y. Gao, and S. V. Levchenko, Single-Atom alloy catalysts designed by first-principles calculations and artificial intelligence, *Nat. Commun.* **12**, 1833 (2021).
- [23] C. Wang, X. Wang, T. Zhang, P. Qian, T. Lookman, and Y. Su, A descriptor for the design of 2D MXene hydrogen evolution reaction electrocatalysts, *J. Mater. Chem. A* **10**, 18195 (2022).
- [24] G. Kresse and D. Joubert, From ultrasoft pseudopotentials to the projector augmented-wave method, *Phys. Rev. B* **59**, 1758 (1999).
- [25] J. P. Perdew, K. Burke, and M. Ernzerhof, Generalized Gradient Approximation Made Simple, *Phys. Rev. Lett.* **77**, 3865 (1996).
- [26] P. E. Blöchl, Projector augmented-wave method, *Phys. Rev. B* **50**, 17953 (1994).
- [27] R. Dronskowski and P. E. Blöchl, Crystal orbital Hamilton populations (COHP). Energy-Resolved visualization of chemical bonding in solids based on density-functional calculations, *J. Phys. Chem.* **97**, 8617 (1993).
- [28] R. Nelson, C. Ertural, J. George, V. L. Deringer, G. Hautier, and R. Dronskowski, LOBSTER: Local orbital projections, atomic charges, and chemical-bonding analysis from projector-augmented-wave-based density-functional theory, *J. Comput. Chem.* **41**, 1931 (2020).
- [29] J. K. Nørskov, T. Bligaard, A. Logadottir, J. R. Kitchin, J. G. Chen, S. Pandelov, and U. Stimming, Trends in the exchange current for hydrogen evolution, *J. Electrochem. Soc.* **152**, J23 (2005).
- [30] J. Greeley, T. F. Jaramillo, J. Bonde, I. Chorkendorff, and J. K. Nørskov, Computational high-throughput screening of electrocatalytic materials for hydrogen evolution, *Nat. Mater.* **5**, 909 (2006).
- [31] See Supplemental Material at <http://link.aps.org/supplemental/10.1103/PhysRevMaterials.7.085801> for four samples for the calculation of $\Delta E_{ZPE} - T\Delta S_H$; Mo_2CO_2 free energies of three types of O atom sites; ΔG_H for Mo_2CO_2 (DFT-D3); descriptor subsets using KRR model on Mo_2CO_2 -STM; descriptor subsets using KRR model on W_2CO_2 -STM; -ICOHP of samples in $Mo_3C_2O_2$ -STM and $Mo_4C_3O_2$ -STM; ΔG_H vs pH; PDOS of Mo_2CO_2 -STM, Ti_2CO_2 -STM, and Zr_2CO_2 -STM; COHP and -ICOHP values of Mo_2CO_2 -STM; relational graphs between ΔG_H and typical descriptors; Pearson's correlation coefficients between ΔG_H and input descriptors; feature selection for Mo_2CO_2 -STM and W_2CO_2 -STM; ΔG_H predicted by the Gaussian process regression (GPR) model with five key descriptors; $\Delta G_{H-DFT-D3}$ vs ΔG_{H-PBE} ; exchange current description of Mo_2CO_2 -STM, which also includes Refs. [29,39-43].
- [32] V. Vovk, Kernel Ridge Regression, in *Empirical Inference: Festschrift in Honor of Vladimir N. Vapnik*, edited by B. Schölkopf, Z. Luo, and V. Vovk (Springer, Berlin, 2013), pp. 105-116.
- [33] T. Hofmann, B. Schölkopf, and A. J. Smola, Kernel methods in machine learning, *Ann. Stat.* **36**, 1171 (2008).

- [34] F. Pedregosa, G. Varoquaux, A. Gramfort, V. Michel, B. Thirion, O. Grisel, M. Blondel, P. Prettenhofer, R. Weiss, V. Dubourg *et al.*, Scikit-Learn: Machine learning in Python, *J. Mach. Learn. Res.* **12**, 2825 (2011).
- [35] G. Gao, A. P. O'Mullane, and A. Du, 2D MXenes: A new family of promising catalysts for the hydrogen evolution reaction, *ACS Catal.* **7**, 494 (2017).
- [36] Y. W. Cheng, J. H. Dai, Y. M. Zhang, and Y. Song, Two-Dimensional, ordered, double transition metal carbides (MXenes): A new family of promising catalysts for the hydrogen evolution reaction, *J. Phys. Chem. C* **122**, 28113 (2018).
- [37] M. López, K. S. Exner, F. Viñes, and F. Illas, Computational Pourbaix diagrams for MXenes: A key ingredient toward proper theoretical electrocatalytic studies, *Adv. Theory Simul.* **2200217** (2022).
- [38] H. Ooka, M. E. Wintzer, and R. Nakamura, Non-Zero binding enhances kinetics of catalysis: Machine learning analysis on the experimental hydrogen binding energy of platinum, *ACS Catal.* **11**, 6298 (2021).
- [39] K. S. Exner, Is thermodynamics a good descriptor for the activity? Re-Investigation of Sabatier's principle by the free energy diagram in electrocatalysis, *ACS Catal.* **9**, 5320 (2019).
- [40] K. S. Exner, Does a thermoneutral electrocatalyst correspond to the apex of a volcano plot for a simple two-electron process?, *Angew. Chem. - Int. Ed.* **59**, 10236 (2020).
- [41] H. Ooka and R. Nakamura, Shift of the optimum binding energy at higher rates of catalysis, *J. Phys. Chem. Lett.* **10**, 6706 (2019).
- [42] A. R. Zeradjanin, P. Narangoda, J. Masa, and R. Schlögl, What controls activity trends of electrocatalytic hydrogen evolution reaction? Activation energy versus frequency factor, *ACS Catal.* **12**, 11597 (2022).
- [43] P. Lindgren, G. Kastlunger, and A. A. Peterson, A challenge to the $G \sim 0$ interpretation of hydrogen evolution, *ACS Catal.* **10**, 121 (2020).
- [44] L. M. Ghiringhelli, J. Vybiral, S. V. Levchenko, C. Draxl, and M. Scheffler, Big Data of Materials Science: Critical Role of the Descriptor, *Phys. Rev. Lett.* **114**, 105503 (2015).
- [45] C. Robert, Machine learning, a probabilistic perspective, *Chance* **27**, 62 (2014).
- [46] W. Jiang, X. Zou, H. Du, L. Gan, C. Xu, F. Kang, W. Duan, and J. Li, Universal descriptor for large-scale screening of high-performance MXene-based materials for energy storage and conversion, *Chem. Mater.* **30**, 2687 (2018).
- [47] N. Ran, W. Qiu, E. Song, Y. Wang, X. Zhao, Z. Liu, and J. Liu, Bond electronegativity as hydrogen evolution reaction catalyst descriptor for transition metal (TM = Mo, W) dichalcogenides, *Chem. Mater.* **32**, 1224 (2020).
- [48] J. Liu, H. Liu, H. Chen, X. Du, B. Zhang, Z. Hong, S. Sun, and W. Wang, Progress and challenges toward the rational design of oxygen electrocatalysts based on a descriptor approach, *Adv. Sci.* **7**, 1901614 (2020).
- [49] A. P. Bartók, R. Kondor, and G. Csányi, On representing chemical environments, *Phys. Rev. B* **87**, 184115 (2013).
- [50] F. Faber, A. Lindmaa, O. A. Von Lilienfeld, and R. Armiento, Crystal structure representations for machine learning models of formation energies, *Int. J. Quantum Chem.* **115**, 1094 (2015).
- [51] J. Liu, C. Tang, Z. Ke, R. Chen, H. Wang, W. Li, C. Jiang, D. He, G. Wang, and X. Xiao, Optimizing hydrogen adsorption by *d*-orbital modulation for efficient hydrogen evolution catalysis, *Adv. Energy Mater.* **12**, 2103301 (2022).
- [52] S. M. Lundberg and S.-I. Lee, A Unified Approach to Interpreting Model Predictions, in *Advances in Neural Information Processing Systems*, edited by I. Guyon, U. V. Luxburg, S. Bengio, H. Wallach, R. Fergus, S. Vishwanathan, and R. Garnett (Curran Associates, Inc., New York, 2017), Vol. 30, pp. 4765–4774.
- [53] Z. J. Zhao, S. Liu, S. Zha, D. Cheng, F. Studt, G. Henkelman, and J. Gong, Theory-Guided design of catalytic materials using scaling relationships and reactivity descriptors, *Nat. Rev. Mater.* **4**, 792 (2019).
- [54] J. K. Nørskov, Electronic factors in catalysis, *Prog. Surf. Sci.* **38**, 103 (1991).
- [55] C. Ling, L. Shi, Y. Ouyang, and J. Wang, Searching for highly active catalysts for hydrogen evolution reaction based on *O*-terminated MXenes through a simple descriptor, *Chem. Mater.* **28**, 9026 (2016).